Research Article | Vol. 27, No. 16 | 5 Aug 2019 | OPTICS EXPRESS 22939
Optics EXPRESS

Plasmon resonances in coupled Babinet complementary arrays in the mid-infrared range

GOEKALP ENGIN AKINOGLU,[1,2] ESER METIN AKINOGLU,[3,4] KRZYSZTOF KEMPA,[3,5] AND MICHAEL GIERSIG[1,3,*]

[1]*Freie Universität Berlin, Department of Physics, 14195 Berlin, Germany*
[2]*Advanced Materials and BioEngineering Research Centre (AMBER) and School of Chemistry, Trinity College Dublin, The University of Dublin, Dublin, Ireland*
[3]*International Academy of Optoelectronics at Zhaoqing, South China Normal University, Zhaoqing, 526238 Guangdong, China*
[4]*ARC Centre of Excellence in Exciton Science, School of Chemistry, University of Melbourne, Parkville, VIC 3010, Australia*
[5]*Boston College, Department of Physics, Chestnut Hill, Massachusetts 02467, USA*
**giersig@physik.fu-berlin.de*

Abstract: A plasmonic structure with transmission highly tunable in the mid-infrared spectral range is developed. This structure consists of a hexagonal array of metallic discs located on top of silicon pillars protruding through holes in a metallic Babinet complementary film. We reveal with FDTD simulations that changing the hole diameter tunes the main plasmonic resonance frequency of this structure throughout the infrared range. Due to the underlying Babinet physics of these coupled arrays, the spectral width of these plasmonic resonances is strongly reduced, and the higher harmonics are suppressed. Furthermore, we demonstrate that this structure can be easily produced by a combination of the nanosphere lithography and the metal-assisted chemical etching technique.

1. Introduction

Complementary vertically coupled plasmonic arrays (VCPAs) were first studied by Li et al. [1]. In general, these VCPAs have a structure that can be described as two displaced, complementary plasmonic slabs. These plasmonic slabs consist of (*i*) a plasmon active metal film with submicron sized and periodically ordered perforations, and (*ii*) complementary, periodically ordered plasmon active antennas. Typically, the size and shape of the discs are exactly complementary to the voids in the perforated film, though there exist examples of not strictly complementary VCPAs [2,3]. The geometrical dimensions of these systems dictate and enable a designed complex optical response. Whereas the displacement of the two slabs determines their coupling strength, the resonance is also greatly influenced by the perforation size and shape, the array period (pitch), as well as by array symmetry. Matching the geometric dimensions carefully, a spectral window of extraordinarily optical transmission (EOT) can be engineered [4–7]. The effect is based on the fundamental surface plasmon excitation of periodically perforated thin metal films [4]. Several potential applications have been proposed. For instance, the underlying physical phenomena governing the optical response of VCPAs have been exploited in the context of color printing, where individual color pixels can be fabricated beyond the diffraction limit [8–11]. Furthermore, VCPA were used as plasmonic sensors for surface enhanced Raman spectroscopy [1,12,13], surface enhanced infrared spectroscopy [14], surface enhanced fluorescence spectroscopy [15] and plasmonic refractive index sensing [2,3,16]. Often, VCPAs with anisotropic structure are used which exhibit polarization dependency in their optical response [9,14,17]. In general, the VCPAs reported to date were commonly fabricated using very sophisticated lithography

#363630 https://doi.org/10.1364/OE.27.022939
Journal © 2019 Received 28 Mar 2019; revised 11 Jun 2019; accepted 20 Jun 2019; published 26 Jul 2019

Optics EXPRESS

methods such as electron beam lithography [1,10,11], which is associated with high costs, low throughput and small obtainable areas.

Here, we investigate vertically coupled Babinet complementary VCPAs, and explore their optical properties in the infrared (IR) frequency range, including mid-IR. The simulation of the electromagnetic response is achieved with the Finite Difference Time Domain (FDTD) code, and enables prediction of an EOT window by controlling geometrical parameters of the arrays. Our proposed structures can easily be fabricated combining the nanosphere lithography (NSL) and metal assisted etching techniques [18,19]. An important advantage of this design is that it avoids the use of infrared absorbing polymers and ceramics, which otherwise superpose with signals in the desired frequency range. Due to the nature of the Babinet complementary arrays, higher harmonics of the resonances are suppressed, which is an attractive feature for smart window applications.

2. Materials and methods

2.1. Sample fabrication

To test the feasibility of the NSL sample fabrication [20], we made a prototype of the proposed Babinet VCPA structure. Fabrication steps are sketched in Fig. 1(a)–(c). First, a hcp monolayer of polystyrene (PS) particles (784 nm diameter) is assembled on an undoped silicon wafer, using the technique described in [19]. Next, the PS particle diameters are reduced to 642 nm in an oxygenated plasma, while maintaining their position. This process is highly dependent on the employed plasma parameters [21]. The non-closed packed array of shrank PS spheres is then used as a template to deposit 20 nm gold, with a home-build physical vapor deposition system at 10^{-6} mbar, and subsequently the PS particles are removed by ultrasonication in toluene. The schematic of the resulting structure is shown in Fig. 1(a) and in the SEM picture in Fig. 1(d). Then, the hole array undergoes metal assisted chemical etching in a 2:5:12 H_2O_2 (35%):HF(40%): H_2O solution, where the length of the hexagonally ordered silicon nanopillars can be varied by the etching time [22–24]. The resulting structure is a gold film, with an array of circular holes caused by the protruding silicon pillars (Fig. 1(b) and Fig. 1(e)). Finally, the array is coated with an additional 30 nm thick layer of gold, yielding a complementary array of discs on top of the pillars (Fig. 1(c)). Figure 1(f) shows an SEM image of such a fabricated structure.

2.2. Simulations

FDTD simulations of the sample transmission were performed with the software package MEEP [25]. A broadband gaussian pulse is used to probe the transmitted flux, whereas the transmittance spectra are normalized to the incident light. The employed geometry represents the hexagonal VCPA obtained experimentally. The array period/pitch is a, disk diameter (also equal to the perforation diameter) is d, and the silicon pillar height (equal to the array displacement) is h. The source plane is placed inside the silicon, and the transmittance flux plane on the opposite side of the interface. The structure was periodically extended using the periodic boundary condition (PBC), whereas artificial absorber layers hinder unwanted back reflections. The dielectric function of the gold was taken from Ref [26], and the silicon substrate was modeled dispersionless, with the refractive index of $n = 3.4$. The thickness of the gold film was set to 50 nm for the hole array slab, and 30 nm for the disk slab.

2.3. Sample characterization

Fourier Transformed Infrared Spectra (FTIR) were measured with a Hyperion 2000 (Brurker) infrared microscope equipped with a $\times 15$, 0.4 NA Schwarzschild objective and connected to a 80V Vertex (Brurker) spectrometer. Transmission spectra were taken with 40 kHz mirror velocity and 250 spectra were averaged of $100\,\mu m \times 100\,\mu m$ area to obtain the final result.

Optics EXPRESS

3. Results and discussion

A schematic diagram depicting the sample fabrication is shown in Fig. 1, and representative Scanning Electron Microscopy (SEM) images of VCPA structures taken at a 30° angle (Fig. 1(f)) and from cross-section view with two different pillar heights/lengths are shown in Figs. 2(a) and 2(b). Pillar length fluctuations are visible and affect the FTIR spectra shown in Fig. 2(c), by significantly broadening the resonant transmission peaks, as compared to simulations which assume no pillar length fluctuations. However, the shown simulated peak shifts for shorter (75 nm) and longer (85 nm) pillars strongly suggest the inhomogeneous nature of the experimental peak/line broadening. The average maximum locations agree well with the experimental result. An additional broadening is due to the fact that the deposited metal was not fully crystalized, while the gold data used in simulations were taken from Ref [26]. based on well-crystallized Au samples. Similar differences between simulated and measured spectra occur for other VCPA structures. The simulation model and main simulation results are shown in Fig. 3. Figure 3(b) shows the optical response of the studied Babinet VCPAs in respect to the variations of d, while $a = 784\,\text{nm}$ and $h = 200\,\text{nm}$ were fixed. Pronounced transmission peaks are observed, with a significant red shift with increasing disk diameter, and almost constant transmission intensity. This relationship is consistent with reports for VCPAs in cubic symmetry [6], and can also be observed in periodically perforated thin metal films [5]. Furthermore, a shoulder on the transmission peak can be observed at the low wavelength side [27]. To investigate the origin of this feature, we performed additional simulations of the reference systems, which we discuss in more detail below.

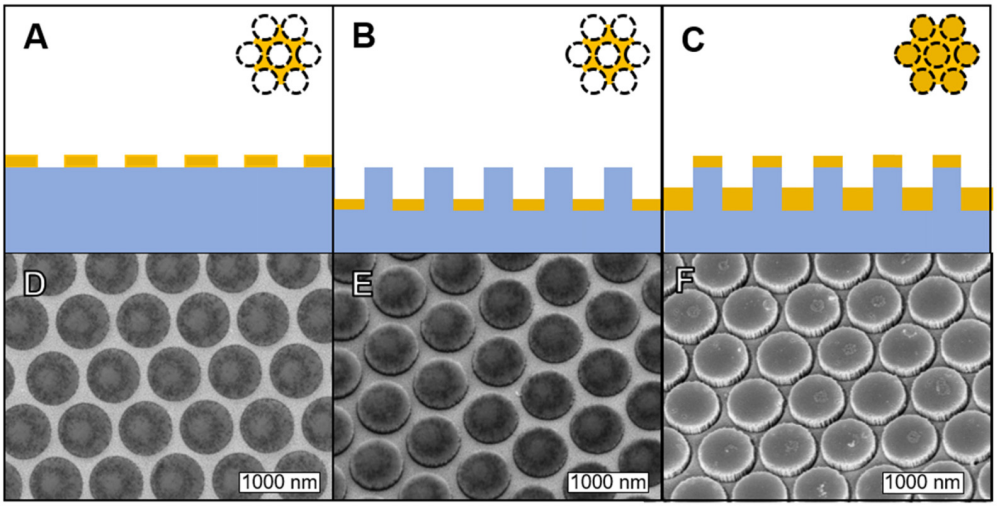

Fig. 1. (A – C) Schematic presentation of the processing steps in the VCPA fabrication. (D) SEM image of the gold hole array, (E) after metal assisted etching and (F) after VCPA formation.

Optics EXPRESS

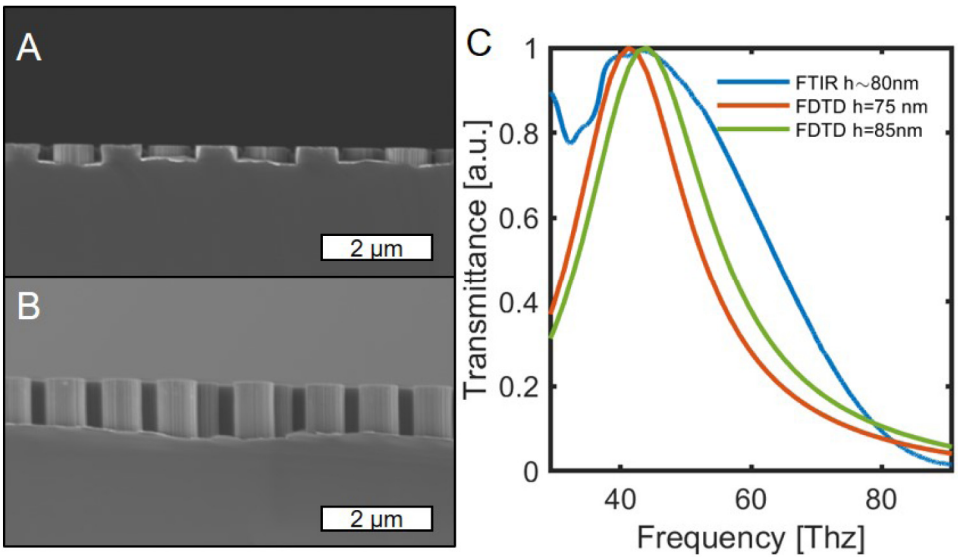

Fig. 2. (A - B) SEM images of the cross-sections of two fabricated VCPA structures, with different pillar heights. (C) Normalized experimental (FTIR) result for one of our VCPA structures is shown as a solid blue line. Red and green solid lines are for our FDTD simulated results.

Transmittance spectra for varying array pitch a, while $h = 200\,\text{nm}$ and $d = 627\,\text{nm}$ were kept constant are shown in Fig. 3(c). Clearly, the location of the main peaks is almost unchanged by the variation of a, with only a small redshift for a approaching d [28]. Figure 2(d) shows the dependence of the transmittance on the pillar height h, while $a = 784\,\text{nm}$ and $d = 627\,\text{nm}$ are fixed. The main result is that a significant red shift of the plasmonic resonance occurs for small $h < 150\,\text{nm}$. This red shift is a result of increased plasmonic coupling between the arrays, similar to the gap size dependent resonance of plasmonic dimers [28]. For $h > 200\,\text{nm}$ a shoulder appears at shorter wavelength next to the plasmonic resonance. Because $\lambda >> d$, a simple long wavelengths, effective medium approach can be used to obtain a qualitative understanding of the spectra. The complicated structures (arrays) can be simply viewed as uniform layers with some effective dielectric functions. In the simplest version of this approach, one could use only two, decoupled separate layers: the discs, and the film of complementary holes. Then, the response of the complementary array on holes could be obtained simply from the Babinet's principle, which says that the corresponding transmittances obey the following relation [29]:

$$T_{disc} + T_{holes} = 1 \tag{1}$$

Since in the effective medium limit both layers can be considered uniform, one can write the total transmittance through the bi-layer as [29]

$$T = T_{disc} T_{holes} = T_{disc}\left(1 - T_{disc}\right) = T_{disc} - \left(T_{disc}\right)^2 \tag{2}$$

where we eliminated T_{holes} by using Eq. (1). In the range where T_{disc} is small, Eq. (2) leads to a rough estimate $T \approx T_{disc}$, i.e. the total transmittance of the bilayer is dominated by the behavior of the discs. For example, the resonances in Fig. 3(b) can be understood in terms of the surface plasmon "whispering gallery" modes, induced on the circumferences of the discs, similarly to those observed by Peng et al. [30]. Since the mid-IR wavelengths lie well above of the surface plasmon saturation wavelength of gold (~500 nm), the resonating surface plasmons are in the retarded limit, i.e. their dispersion closely follows the photon light line

Optics EXPRESS

[29]. Therefore finally, after ignoring the inter-disc interaction, we find the following estimate of the wavelengths at the transmittance maxima

$$\lambda_{max} \approx \lambda_{pl} = \pi d\sqrt{\varepsilon} \tag{3}$$

Where λ_{pl} is the wavelength of the surface plasmon, and the background dielectric constant is $\varepsilon \approx (1+\varepsilon_{Si})/2$. As shown in Fig. 4, this very rough estimate (linear dependency of the peak positions on d) agrees well with the simulated results.

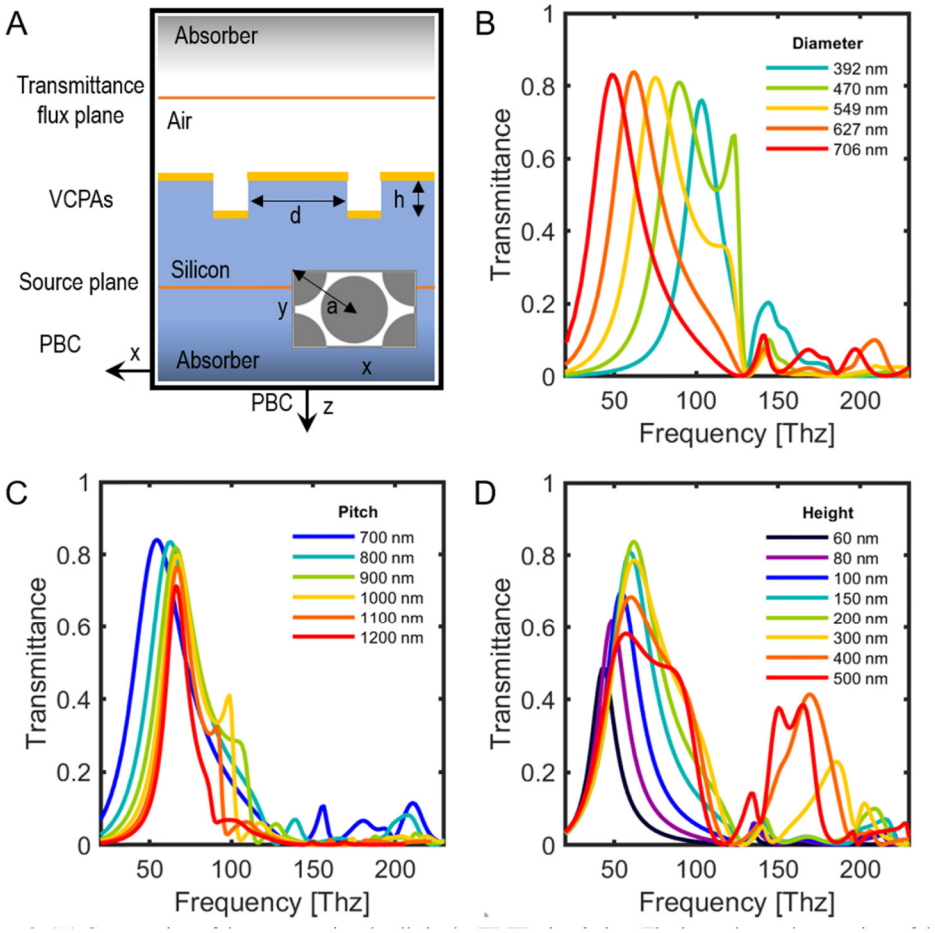

Fig. 3. (A) Crosssection of the computational cells in the FDTD simulation. The inset shows the top view of the simulation cell. (B) Transmittance spectra for different d, and fixed $h = 200\,\text{nm}$ and $a = 784\,\text{nm}$. (C) Transmittance spectra for different a, and fixed $h = 200\,\text{nm}$ and $d = 627\,\text{nm}$. (D) Transmittance spectra for different h, and fixed $a = 784\,\text{nm}$ and $d = 627\,\text{nm}$.

The approximate analysis above implies that the Babinet complementary arrays do not interact. While this assumption captures qualitatively the main physics, due to the very short pillars (ultra-short inter-array distance), some interaction is present. In addition, the pillars are made of strongly polarizable medium, and thus can sustain modes by themselves. These additional effects can be treated numerically, and we have performed a series of FDTD simulations for various systems containing our Babinet complementary arrays. Firstly, we simulate separately the arrays of discs and holes on a flat Si surface, to test Eq. (1). Figure 5

Optics EXPRESS

shows that indeed, apart from the shift resulting from Si reflection, the disc and hole array transmission spectra have the characteristic anti-symmetric character, with the transmission maxima (minima) of hole array, occurring at transmission minima (maxima) of the disc array, respectively. This is the characteristic behavior of the Babinet complementary arrays, as discussed in detail in [29].

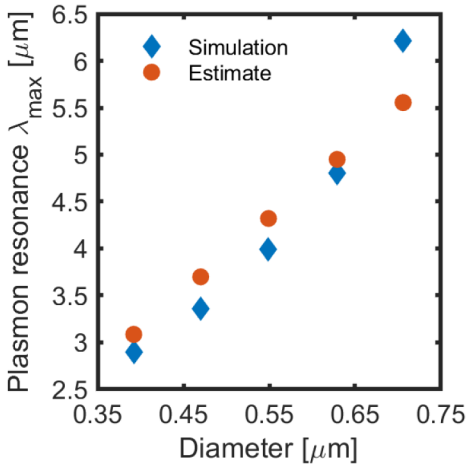

Fig. 4. Comparison between simulated and estimated plasmon resonance position.

Next, we consider the arrays of pillars with various metal arrangements. Figure 6 shows the results for structures with various pillar diameters *d*. Similar results for varying *a* and *h* are given in the appendix. Figure 6(a) shows spectra of the Si pillars alone, without any metallic layers. The spectrum is free of resonances for large wavelengths, but contains multiple resonance peaks below 2500 nm wavelengths. These peaks are due to the lattice periodicity, as can be verified by changing *a* (appendix). Figure 6(b) shows transmittance spectra for the same array of pillars, but with gold discs on their tops and no metal below, between pillars. These spectra resemble those in Fig. 6(d), which are for the complete structure of the coupled hole-disc arrays. This validates the approximate result derived above $T \approx T_{disc}$. This is further justified by Fig. 6(c), which shows spectra of the pillars, this time with gold residing only between pillars. Since this hole array, only very roughly represents the Babinet complementary of the discs on pillars, only a very rough qualitative Babinet asymmetry of this spectrum and that shown in Fig. 6(b) occurs, at least for large pillar diameters.

Figure 6(d) shows transmittance spectra of our completed VCPA, the same data as those in Fig. 2(b), but plotted vs wavelength to emphasize the spectral features in the low frequency region. Two features are clear in these spectra: sharpening of the broad-asymmetric peaks for large wavelengths $>3000\,\text{nm}$, and suppression of sharp-symmetric transmission peaks at small wavelengths $<2000\,\text{nm}$. Both effects are hidden in Eq. (2). To show that, consider first a simple model of T_{disc}, which roughly resembles the step-like line (for $d=706\,\text{nm}$) in Fig. 6(b):

$T_{disc}=0$ for $\lambda<\lambda_0$, and $T_{disc}=1-exp\left(-\beta\left(\lambda-\lambda_0\right)\right)$ for $\lambda\geq\lambda_0$, where $\lambda_0=2500\,nm$. After inserting this into Eq. (2) one gets $T=\left[1-exp\left(-\beta\left(\lambda-\lambda_0\right)\right)\right]exp\left(-\beta\left(\lambda-\lambda_0\right)\right)$ which has a well-defined peak, with maximum located at $\lambda_{max}=\lambda_0+\ln 2/\beta$. To illustrate the second effect, we assume that $T_{disc}=\delta_{\lambda-\lambda_i}$, i.e. it is a very sharp symmetric resonance represented by a Kronecker delta.

Optics EXPRESS

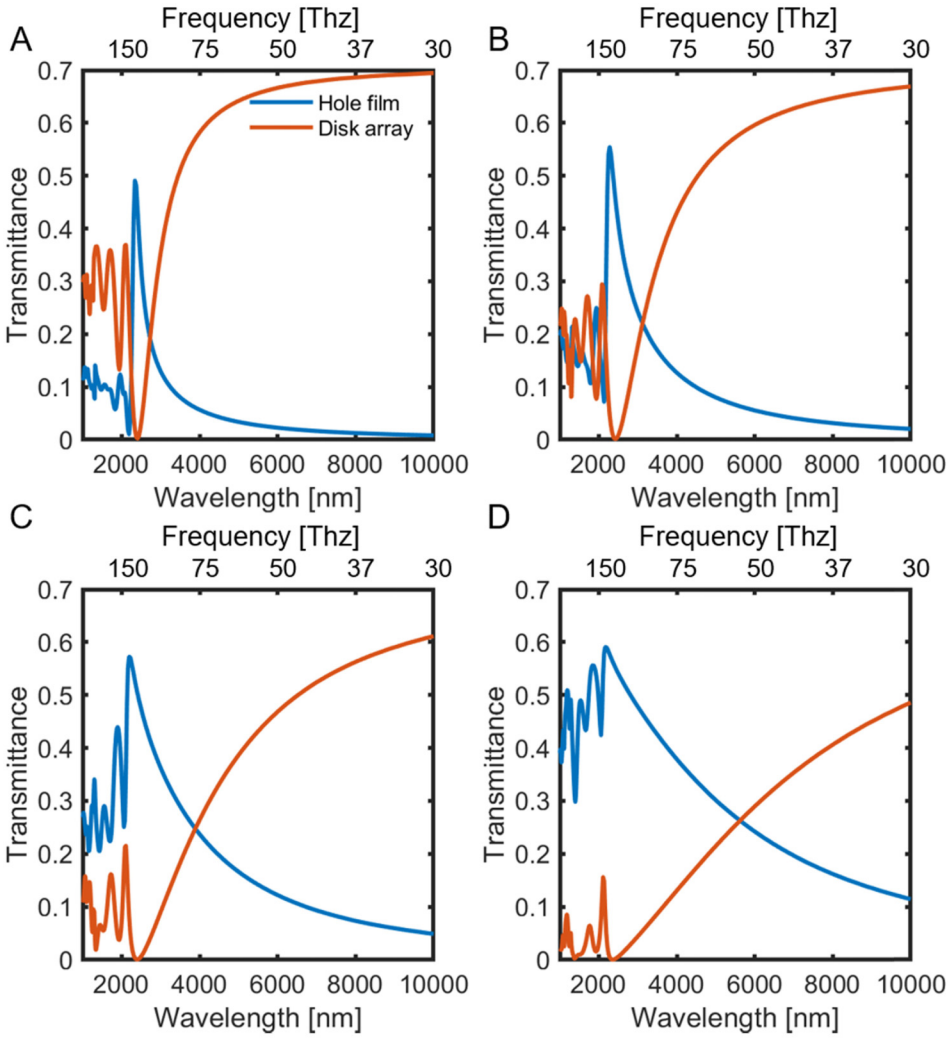

Fig. 5. Babinet complementary arrays of holes (blue lines) and discs (red lines) on Si for various d and fixed $a = 784nm$. (A) 470 nm (B) 549 nm (C) 627 nm (D) 706 nm.

After inserting to Eq. (2), one gets $T = 0$, i.e. a complete suppression of that peak in this model. This effect has been employed in a design of a somewhat similar VCPA structure used to covertly encode images [31].

4. Conclusion

The optical properties of hexagonal ordered vertically coupled plasmonic arrays were investigated in the infrared range. The VCPAs exhibit an extra ordinary transmission at a plasmon resonance. We show by simulation and an analytical estimate, that the main control parameter for the plasmonic response is the pillar diameter. In the interaction domain, plasmon resonance maxima redshift with decreasing distances between discs and the complementary holes. Due to the underlying Babinet physics of these coupled arrays, the spectral width of these plasmonic resonances is strongly reduced, and the higher harmonics are suppressed. Also, we demonstrate that this structure can be easily produced by a combination of the nanosphere lithography and the metal assisted chemical etching. These are attractive features for device applications.

Optics EXPRESS

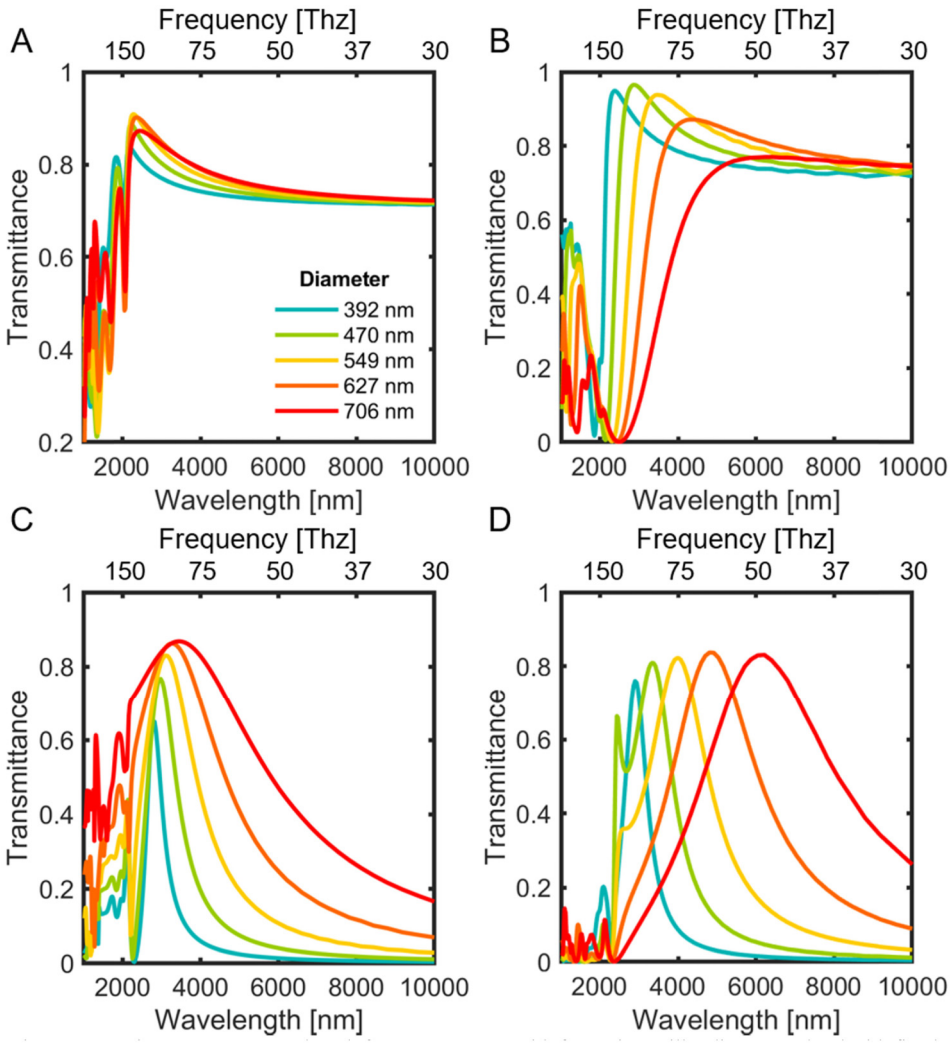

Fig. 6. Transmittance versus wavelength for our structures with for various pillar diameters d and with fixed $h = 200\,\text{nm}$ and $a = 784\,\text{nm}$. (A) pillars alone, (B) gold discs on top of pillars, (C) gold only on the bottom, with pillars protruding (no discs), and (D) structure with both arrays present: discs on top of pillars, and the Babinet complementary array at the pillar bottom.

5. Appendix

To investigate the origin of the VCPAs resonances at wavelengths below 2500 nm, we performed calculations of reference systems, i.e. the same geometries without any plasmonic slabs and with only one of both plasmonic slabs respectively (Fig. 7). A complex photonic response can be observed for hexagonally ordered silicon pillar arrays without plasmonic slabs (Fig. 7(a)) with several maxima and minima for small wavelengths. Clearly, the resonances blue shift for smaller pitches and the amplitude becomes more pronounced. These features have previously been assigned to different photonic modes and appear throughout all spectra. The optical response with metal discs atop the silicon pillars shows a plasmon resonance which appears as a minimum in transmission with red shift for increasing a (Fig. 7(b)). The photonic modes appear as superpositions on the plasmonic resonance. The optical response of the perforated metal film embedded into the foundation between the silicon pillar

Optics EXPRESS

arrays is shown in Fig. 7(c). Peaks assigned to extraordinary enhanced transmission are observed on the low wavelength side together with superposed minima originating from the photonic modes of the silicon pillar arrays. The dependence of the VCPA optical resonance on the diameter is shown in Fig. 7(d).

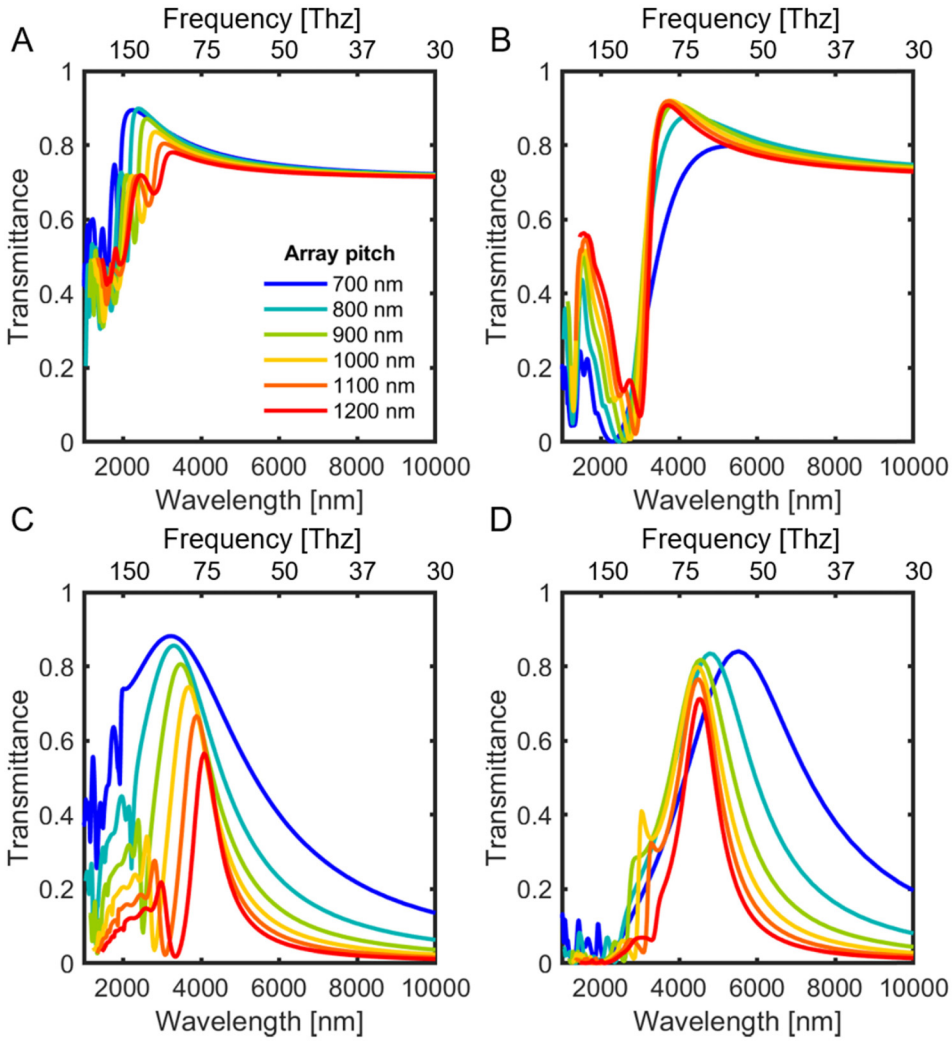

Fig. 7. Transmittance versus wavelength for our structures with for various array pitches a and with fixed $h = 200\,\text{nm}$ and $d = 627\,\text{nm}$. (A) pillars alone, (B) gold discs on top of pillars, (C) gold only on the bottom, with pillars protruding (no discs), and (D) structure with both arrays present: discs on top of pillars, and the Babinet complementary array at the pillar bottom.

They exhibit a plasmon resonance independent of the pitch diameter for large enough separation of the individual pillars and the photonic modes appear as shoulders or as a small modulation of the main resonance for small wavelengths. Finally, the optical response in dependence of the pillar height is shown in Fig. 8. The spectra for the silicon pillars are governed by photonic modes below 2500 nm and a strong transmission appearing at around 2500 nm (Fig. 8(a)). The main maxima red shifts with larger pillar heights and the absolute transmission reaches up to 100%. A system with discs on top of the pillars (Fig. 8(b)) and a perforated gold film at the base of the film (Fig. 8(c)) shows a strong superposition of the main maxima with the plasmonic response. The optical response of the VCPAs dependends

Optics EXPRESS

on the pillar height (Fig. 8(d)) where the photonic mode appears as shoulder on thw low wavelength side of the plasmon resonance.

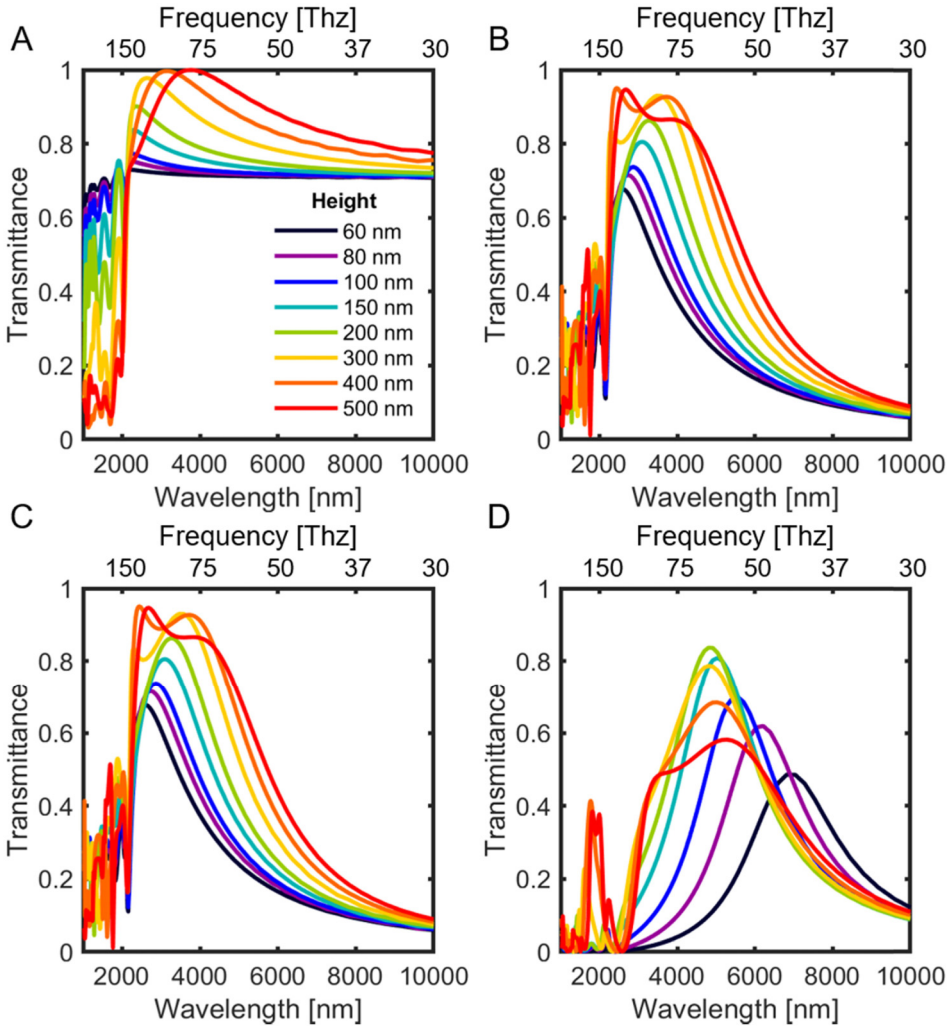

Fig. 8. Transmittance versus wavelength for our structures with for various pillar heights h and with fixed $a = 784\,\text{nm}$ and $d = 627\,\text{nm}$. (A) pillars alone, (B) gold discs on top of pillars, (C) gold only on the bottom, with pillars protruding (no discs), and (D) structure with both arrays present: discs on top of pillars, and the Babinet complementary array at the pillar bottom.

Funding

Alexander von Humboldt Stiftung; Guangdong Province Introduction of Innovative R&D Team (2016ZT06C517); Centre of Excellence in Exciton Science, Australian Research Council (CE170100026).

Acknowledgements

The authors gratefully thank the Freie Universität Berlin Physics IT department for access to their hpc-clusters and Joachim Heberle for usage of his Infrared spectrometer and microscope. E.M.A. thankfully acknowledges a Feodor Lynen Research Fellowship by the Alexander von Humboldt Foundation.

Optics EXPRESS

References

1. W.-D. Li, F. Ding, J. Hu, and S. Y. Chou, "Three-dimensional cavity nanoantenna coupled plasmonic nanodots for ultrahigh and uniform surface-enhanced Raman scattering over large area," Opt. Express **19**(5), 3925–3936 (2011).
2. W. Li, X. Jiang, J. Xue, Z. Zhou, and J. Zhou, "Antibody modified gold nano-mushroom arrays for rapid detection of alpha-fetoprotein," Biosens. Bioelectron. **68**, 468–474 (2015).
3. Y. Shen, J. Zhou, T. Liu, Y. Tao, R. Jiang, M. Liu, G. Xiao, J. Zhu, Z.-K. Zhou, X. Wang, C. Jin, and J. Wang, "Plasmonic gold mushroom arrays with refractive index sensing figures of merit approaching the theoretical limit," Nat. Commun. **4**(1), 2381 (2013).
4. T. W. Ebbesen, H. J. Lezec, H. F. Ghaemi, T. Thio, and P. A. Wolff, "Extraordinary optical transmission through sub-wavelength hole arrays," Nature **391**(6668), 667–669 (1998).
5. W.-D. Li, J. Hu, and S. Y. Chou, "Extraordinary light transmission through opaque thin metal film with subwavelength holes blocked by metal disks," Opt. Express **19**(21), 21098–21108 (2011).
6. Q. Zhang, P. Hu, and C. Liu, "Giant-enhancement of extraordinary optical transmission through nanohole arrays blocked by plasmonic gold mushroom caps," Opt. Commun. **335**, 231–236 (2015).
7. F. Fan, M. Chen, S. Chen, X. H. Wang, and S. J. Chang, "Complementary Plasmonic Arrays for Extraordinary Transmission and Modulation of Terahertz Wave," IEEE Photonics Technol. Lett. **27**(23), 2485–2488 (2015).
8. Y. Gu, L. Zhang, J. K. W. Yang, S. P. Yeo, and C.-W. Qiu, "Color generation via subwavelength plasmonic nanostructures," Nanoscale **7**(15), 6409–6419 (2015).
9. C. Williams, G. Rughoobur, A. J. Flewitt, and T. D. Wilkinson, "Nanostructured plasmonic metapixels," Sci. Rep. **7**(1), 7745 (2017).
10. R. Mudachathi and T. Tanaka, "Up Scalable Full Colour Plasmonic Pixels with Controllable Hue, Brightness and Saturation," Sci. Rep. **7**(1), 1199 (2017).
11. K. Kumar, H. Duan, R. S. Hegde, S. C. W. Koh, J. N. Wei, and J. K. W. Yang, "Printing colour at the optical diffraction limit," Nat. Nanotechnol. **7**(9), 557–561 (2012).
12. J. D. Caldwell, O. Glembocki, F. J. Bezares, N. D. Bassim, R. W. Rendell, M. Feygelson, M. Ukaegbu, R. Kasica, L. Shirey, and C. Hosten, "Plasmonic Nanopillar Arrays for Large-Area, High-Enhancement Surface-Enhanced Raman Scattering Sensors," ACS Nano **5**(5), 4046–4055 (2011).
13. M. Tabatabaei, M. Najiminaini, K. Davieau, B. Kaminska, M. R. Singh, J. J. L. Carson, and F. Lagugné-Labarthet, "Tunable 3D Plasmonic Cavity Nanosensors for Surface-Enhanced Raman Spectroscopy with Sub-femtomolar Limit of Detection," ACS Photonics **2**(6), 752–759 (2015).
14. X. Chen, C. Wang, Y. Yao, and C. Wang, "Plasmonic Vertically Coupled Complementary Antennas for Dual-Mode Infrared Molecule Sensing," ACS Nano **11**(8), 8034–8046 (2017).
15. W. Zhang, F. Ding, W. D. Li, Y. Wang, J. Hu, and S. Y. Chou, "Giant and uniform fluorescence enhancement over large areas using plasmonic nanodots in 3D resonant cavity nanoantenna by nanoimprinting," Nanotechnology **23**(22), 225301 (2012).
16. J. Yuan, H. Z. Cao, Y. Y. Xie, Z. X. Geng, Q. Kan, X. M. Duan, and H. D. Chen, "Gold Elliptic Nanocavity Array Biosensor With High Refractive Index Sensitivity Based on Two-Photon Nanolithography," IEEE Photonics J. **7**(1), 1–8 (2015).
17. C. Wang, Q. Zhang, Y. Song, and S. Y. Chou, "Plasmonic Bar-Coupled Dots-on-Pillar Cavity Antenna with Dual Resonances for Infrared Absorption and Sensing: Performance and Nanoimprint Fabrication," ACS Nano **8**(3), 2618–2624 (2014).
18. J. C. Hulteen and R. P. V. Duyne, "Nanosphere lithography: A materials general fabrication process for periodic particle array surfaces," J. Vac. Sci. Technol. A **13**(3), 1553–1558 (1995).
19. E. M. Akinoglu, A. J. Morfa, and M. Giersig, "Nanosphere lithography-exploiting self-assembly on the nanoscale for sophisticated nanostructure fabrication," Turk. J. Phys. **38**, 563–572 (2014).
20. M. Pisco, F. Galeotti, G. Quero, G. Grisci, A. Micco, L. V. Mercaldo, P. D. Veneri, A. Cutolo, and A. Cusano, "Nanosphere lithography for optical fiber tip nanoprobes," Light Sci. Appl. **6**(5), e16229 (2017).
21. E. M. Akinoglu, A. J. Morfa, and M. Giersig, "Understanding Anisotropic Plasma Etching of Two-Dimensional Polystyrene Opals for Advanced Materials Fabrication," Langmuir **30**(41), 12354–12361 (2014).
22. K. Peng, M. Zhang, A. Lu, N.-B. Wong, R. Zhang, and S.-T. Lee, "Ordered silicon nanowire arrays via nanosphere lithography and metal-induced etching," Appl. Phys. Lett. **90**(16), 163123 (2007).
23. B. Mikhael, B. Elise, M. Xavier, S. Sebastian, M. Johann, and P. Laetitia, "New silicon architectures by gold-assisted chemical etching," ACS Appl. Mater. Interfaces **3**(10), 3866–3873 (2011).
24. A. Cowley, J. Steele, D. Byrne, R. Vijayaraghavan, and P. McNally, "Fabrication and characterisation of GaAs nanopillars using nanosphere lithography and metal assisted chemical etching," RSC Advances **6**(36), 30468–30473 (2016).
25. A. F. Oskooi, D. Roundy, M. Ibanescu, P. Bermel, J. D. Joannopoulos, and S. G. Johnson, "Meep: A flexible free-software package for electromagnetic simulations by the FDTD method," Comput. Phys. Commun. **181**(3), 687–702 (2010).
26. P. B. Johnson and R. W. Christy, "Optical constants of noble metals," Phys. Rev. B **6**, 4370 (1972).
27. C.-H. Sun, P. Jiang, and B. Jiang, "Broadband moth-eye antireflection coatings on silicon," Appl. Phys. Lett. **92**(6), 061112 (2008).

Optics EXPRESS

28. P. Nordlander, C. Oubre, E. Prodan, K. Li, and M. Stockman, "Plasmon hybridization in nanoparticle dimers," Nano Lett. **4**(5), 899–903 (2004).
29. Y. Wang, E. W. Plummer, and K. Kempa, "Foundations of Plasmonics," Adv. Phys. **60**(5), 799–898 (2011).
30. Y. Peng, C. Marcoux, P. Patoka, M. Hilgendorff, M. Giersig, and K. Kempa, "Plasmonics of thin film quasitriangular nanoparticles," Appl. Phys. Lett. **96**(13), 133104 (2010).
31. D. Franklin, S. Modak, A. Vázquez-Guardado, A. Safaei, and D. Chanda, "Covert infrared image encoding through imprinted plasmonic cavities," Light Sci. Appl. **7**(1), 93 (2018).